UHASSELT
KNOWLEDGE IN ACTION

Maastricht University

Faculty of Medicine and Life Sciences
School for Life Sciences
Master of Biomedical Sciences

Master's thesis

Cytoskeletal regulation in phagocytes: Dissecting the roles of diaphanous and nervous wreck in hemocyte functionality

Stijn Van Esser

Thesis presented in fulfillment of the requirements for the degree of Master of Biomedical Sciences, specialization Molecular Mechanisms in Health and Disease

SUPERVISOR :

Prof. dr. Bert BRONE

MENTOR :

Ms Amber DELBROEK

2025
2026

Transnational University Limburg is a unique collaboration of two universities in two countries: the University of Hasselt and Maastricht University.

UHASSELT
KNOWLEDGE IN ACTION

www.uhasselt.be
Universiteit Hasselt
Campus Hasselt:
Martelarenlaan 42 | 3500 Hasselt
Campus Diepenbeek:
Agoralaan Gebouw D | 3590 Diepenbeek

Faculty of Medicine and Life Sciences
School for Life Sciences
Master of Biomedical Sciences

Master's thesis

Cytoskeletal regulation in phagocytes: Dissecting the roles of diaphanous and nervous wreck in hemocyte functionality

Stijn Van Esser

Thesis presented in fulfillment of the requirements for the degree of Master of Biomedical Sciences, specialization Molecular Mechanisms in Health and Disease

SUPERVISOR :

Prof. dr. Bert BRONE

MENTOR :

Ms Amber DELBROEK

Cytoskeletal regulation in phagocytes: Dissecting the roles of diaphanous and nervous wreck in hemocyte functionality*

Stijn Van Esser[1], Amber Delbroek[1,2], Jean-Michel Rigo[1] and Bert Brône[1]

[1]Neurophysiology research group, Biomedical Research Institute, Hasselt University, Campus Diepenbeek, Agoralaan building C - B-3590 Diepenbeek
[2]SYMBIOSE Laboratory, CIRMAP, Research Institute of Biosciences, University of Mons, B-700 Mons, Belgium

*Running title: *Cytoskeletal regulation in hemocytes*

To whom correspondence should be addressed: Bert Brône, Tel: +3211269237; Email: bert.brone@uhasselt.be

Keywords: *Drosophila melanogaster,* phagocytes, actin cytoskeleton, diaphanous, nervous wreck

ABSTRACT

Neurodevelopmental disorders (NDDs) have traditionally been viewed as neuron-centric. However, emerging evidence implicates microglia as key contributors. To perform functions critical to neurodevelopment, including migration, microglia rely on a precise balance between lamellipodia and filopodia formation. This balance is maintained through dynamic actin remodeling. The NDD-risk gene DISC1 has been shown to disrupt this equilibrium, impairing microglial function. Transcriptomic analysis of *Disc1* locus impairment (LI) microglia identified downregulation of *Diaph2* and *Fchsd2*, two actin regulators at opposite ends of the filopodia-lamellipodia equilibrium. Their *Drosophila melanogaster* orthologs, diaphanous (*dia)* and nervous wreck (*nwk*), were therefore investigated with the central aim of determining whether these regulators modulate phagocyte morphology and motility. Addressing this, RNAi-mediated knockdown revealed opposing morphological phenotypes *in vitro*. Depletion of *dia* increased cell circularity and area while suppressing filopodia. Knockdown of *nwk* promoted a filopodia-rich, asymmetric morphology, reflecting a shift in the balance between Arp2/3-mediated branched and formin-driven linear actin polymerization. *In vivo* migration analysis revealed functionally distinct motility profiles consistent with these architectures. *dia*-depleted hemocytes migrated faster, but without directional persistence. *nwk*-depleted hemocytes moved more slowly with increased directional change rate. Attempts to validate the downregulation of *Diaph2* and *Fchsd2* in *Disc1* LI microglia via qPCR were hampered by extremely low transcript abundance. These findings establish distinct roles for *dia* and *nwk* in hemocyte actin regulation with tangible functional consequences for cell motility. Future work should address technical barriers to cross-species translation and explore *Diaph2* and *Fchsd2* as therapeutic targets in microglial-mediated neurodevelopmental pathology.

INTRODUCTION

The development of the central nervous system (CNS) represents an extraordinary feat of biological engineering (1). Spanning from embryonic life into adolescence, neurodevelopment unfolds as a precise, multistep sequence. This process requires a coordinated progression from initial progenitor proliferation and migration to neuronal differentiation and synaptogenesis (2,3). However, for the CNS to achieve functional maturity, this constructive phase must be followed by a critical process of refinement known as stabilization (4,5). This phase is defined by programmed neuronal cell death and the targeted elimination of excess synaptic connections to sculpt precise neuronal circuits.

Dysfunction in these developmental processes alters CNS structure and function. This can ultimately contribute to the etiology of neurodevelopmental disorders (NDDs), including autism spectrum disorder (ASD) and schizophrenia. Clinically, these disorders are characterized by cognitive deficits and behavioral abnormalities (1,6). Traditionally, NDDs are viewed as neuron-centric, where deficits are often attributed to genetic variants

in cytoskeletal proteins (7). Since these proteins form the essential structural framework of neurons, mutations typically result in compromised cellular integrity, impaired intracellular transport, and abnormal synaptic signaling (8,9). Notably, however, cytoskeletal proteins also play pivotal roles in non-neuronal cells, including microglia, the resident phagocytes of the CNS (10).

Microglia play a crucial role during neurodevelopment. They support neurogenesis by releasing trophic factors that aid neuronal survival (11). Furthermore, they perform phagocytosis to clear apoptotic cell debris and execute synaptic pruning, a process that occurs during the stabilization phase of development (11,12). To perform these complex tasks, microglia cannot remain static; they must actively explore their environment, making cellular motility and migration fundamental requirements (13).

The critical engine driving this microglial motility and migration is the dynamic and reversible remodeling of the actin cytoskeleton. This is mediated through receptor-ligand interactions with environmental cues, triggering intracellular signals that result in a process known as actin treadmilling (14). In this process, globular actin (G-actin) monomers polymerize into helical actin filaments (F-actin). These newly created filaments generate force against the cell membrane, driving morphological adaptations and protrusion (15). To achieve functional motility and migration, spatiotemporal coordination between two modes of actin polymerization is required, thereby creating either filopodia or lamellipodia (16).

Lamellipodia are broad, sheet-like structures that provide the primary propulsive force for motility and serve as a scaffold for the structures needed for phagocytic engulfment (17,18). Intracellularly, lamellipodia are composed of a dense network of branched F-actin. The formation of this network is driven by the actin-related protein 2 and 3 (Arp2/3) complex, which initiates nucleation of new branches on the side of actin filaments (19). This process is tightly regulated by the Rho-GTPase Rac1 and its downstream nucleation-promoting factors (NPFs) of the Wiskott-Aldrich syndrome protein family verprolin-homologous protein (WAVE) complex. Activation of Rac1 triggers the WAVE complex, which in turn activates the Arp2/3 complex, facilitating the formation of lamellipodia (20,21). In contrast, filopodia are thin projections that are composed of parallel bundles of unbranched, linear F-actin. Functionally, filopodia serve an exploratory purpose by probing the extracellular environment for chemotactic cues and establishing initial contact with targets (22). The nucleation and elongation of these linear filaments are driven by formins. This pathway is regulated by the Rho-GTPases Cdc42 and RhoA, which activate formins to initiate filament formation (23,24). Efficient microglial function requires a precise balance between the Arp2/3-driven lamellipodia and formin-driven filopodia formation (16).

Disrupted in schizophrenia 1 (DISC1), a major susceptibility gene for NDDs, encodes a cytoskeletal scaffolding protein that regulates neurite outgrowth and synaptic plasticity in neurons during development (25,26). However, its central role within the cytoskeleton led to a recent discovery of its influence within microglia as well (10). Here, DISC1 has emerged as an important modulator of actin dynamics by contributing to the coordination of the switch between lamellipodial Rac1 and filopodial RhoA. Specifically, DISC1 deficiency in microglia skews this balance toward a filopodia-dominant morphology. This structural dysregulation induces microglial hyperphagocytosis, leading to excessive synapse elimination. Consequently, this aberrant synaptic pruning results in diminished excitatory transmission and spatial memory deficits, providing a mechanistic link between microglial cytoskeletal dysfunction and the cognitive hallmarks of NDDs. Despite these profound effects on microglial function, the exact molecular mediators underlying DISC1's pathophysiological role in actin cytoskeleton rearrangement remain unclear. A prior transcriptomic screen using single-cell RNA sequencing on a *Disc1* locus impairment (LI) mouse model identified dysregulation of several genes associated with actin dynamics. Among these, two genes of particular interest were the evolutionarily conserved Diaphanous Related Formin 2 (*Diaph2*) and F-BAR and double SH3 domains protein 2 (*Fchsd2*), both of which were downregulated.

DIAPH2 is a member of the formin family of actin nucleators. After activation by RhoA, it binds to the growing barbed end of the actin filament (27). This interaction shields the

filament from capping proteins that would otherwise terminate growth, while simultaneously recruiting G-actin monomers to accelerate elongation (28). Collectively, this facilitates the acceleration of linear actin filament polymerization, leading to the formation of filopodia (29). FCHSD2 encodes a membrane-binding protein that recruits the Wiskott-Aldrich syndrome protein and SCAR homolog (WASH) complex, another NPF that activates the Arp2/3 complex (30). This triggers the formation of branched actin networks, resulting in lamellipodia (19). Despite these well-defined roles, the precise molecular mechanisms governing their coordination of microglial actin dynamics remain largely undefined. Moreover, the causal link between their dysregulation and the specific cytoskeletal defects observed in *Disc1* LI pathophysiology has yet to be established.

Evaluating the functional roles of these selected candidates in murine models presents significant challenges due to their long generation times and complex breeding strategies for creating transgenic strains. However, the evolutionary conservation of these pathways provides an excellent opportunity to systematically investigate the conserved physiological functions of these candidate genes using *Drosophila melanogaster (D. melanogaster)*. This model's capacity for genetic engineering and its short life cycle provide a rapid, high-throughput platform for studying these actin regulators both *in vitro* and *in vivo* (31). Central to this approach are hemocytes, the professional phagocytes of *D. melanogaster*. As the primary macrophage-like cells in insects, they share highly conserved functional and morphological characteristics with mammalian microglia (32). These phagocytes provide a robust system to dissect the dynamic function of the actin cytoskeleton during migration and phagocytosis. In *D. melanogaster*, diaphanous (*dia*) and nervous wreck (*nwk*) are respectively identified as orthologs of DIAPH2 and FCHSD2 (33,34). These genes mediate analogous cytoskeletal functions in hemocytes, enabling investigation of their roles during *Drosophila* development, particularly during hemocyte migration along the ventral nerve cord (VNC) to shape the emerging nervous system (35).

Therefore, the central aim of this research is to determine whether *dia* and *nwk* modulate phagocyte morphology and motility. Based on their respective roles in linear and branched actin networks, it is hypothesized that knockdown of *dia* and *nwk* in *D. melanogaster* hemocytes alters the balance between Arp2/3 complex and formin-mediated cytoskeletal regulation. Specifically, knockdown of these individual targets is expected to shift cellular morphology toward the extremes of this architectural equilibrium, ultimately impairing phagocyte motility and directional migration. To test this, a GAL4-UAS system will be employed to express RNA interference (RNAi) constructs targeting *dia* and *nwk*, specifically in hemocytes. This will be applied to assess the impact of this knockdown on actin cytoskeletal organization and cell morphology. Additionally, *D. melanogaster* embryos will be utilized for *in vivo* live imaging to track hemocyte migration during development. Ultimately, this research will elucidate key physiological mechanisms, enabling the identification of novel molecular targets within actin regulatory pathways. The development of therapies aimed at these targets could mitigate long-term cognitive and behavioral deficits, thereby improving the quality of life for patients with neurodevelopmental disorders.

EXPERIMENTAL PROCEDURES

Drosophila melanogaster strains – *D. melanogaster* stocks were maintained at 25°C on standard cornmeal-agar under a 12 h light/dark cycle in the UHasselt *Drosophila* facility (established with the support of the Verstreken lab (VIB-KU Leuven, Belgium) and the Wood lab (Edinburgh, Scotland)). Hemocyte-specific gene knockdown was achieved via the GAL4/UAS binary expression system by crossing a srp.hemo-GAL4 driver line (co-expressing GFP, LifeAct-GFP, or H2ACherry) with specific UAS-RNAi responder lines obtained from either the Bloomington Drosophila Stock Center (BDSC) or VIB-KU Leuven. The evaluated experimental genotypes included: srp.hemoGAL4 > GFP, UAS-RNAi-*scar* (positive control), srp.hemoGAL4 > GFP, Yellow Vermillion (Yv^1) (negative control), srp.hemoGAL4 > UAS-RNAi-*LexA* (scramble control), srp.hemoGAL4 > GFP, UAS-RNAi-*dia*, and srp.hemoGAL4 > GFP, UAS-RNAi-*nwk* (targeted gene knockdowns).

Mice strains – Wild-type (WT) and *Disc1* LI mice were generated by breeding heterozygous *Disc1* LI mice (Provided by Prof.

Akira Sawa, Johns Hopkins, Baltimore). Double mutant *Disc1* LI CX3CR1$^{eGFP/eGFP}$ mice, expressing eGFP under the CX3 chemokine receptor 1 promoter to fluorescently label microglia and monocyte-derived cells, were created by in-house breeding. Animals were housed in temperature-and humidity-controlled rooms on a 12h light/dark cycle with *ad libitum* access to food and water. All animal experiments were approved by the Ethics Committee of Hasselt University.

Cell culture – Murine BV2 microglial cells were cultured in Dulbecco's Modified Eagle Medium (DMEM; Sigma-Aldrich, St. Louis, USA), supplemented with 10% heat-inactivated fetal calf serum (FCS; Biowest, Nuaillé, France). Cells were maintained at 37°C in a humidified 5% CO_2 atmosphere and subcultured upon reaching 80-90% confluence using trypsin/EDTA dissociation.

Primary hemocyte isolation – Third-instar *D. melanogaster* larvae were washed sequentially in 1x phosphate-buffered saline (PBS), 70% ethanol, and 1x PBS and transferred to glass coverslips in Schneider's Insect Medium (Sigma-Aldrich, St. Louis, USA) supplemented with 10% FCS, 1% penicillin/streptomycin (P/S, Invitrogen, Carlsbad, USA), and 10 µM phenylthiourea (PTU, Merck, Darmstadt, Germany). Hemolymph was extracted via a small incision in the ventral posterior cuticle using a 27-G needle and allowed to bleed for 1-2 minutes (min). After removing the larvae, hemocytes were adhered to the coverslip at 25°C for 1 hour (h). Coverslips were transferred to a 24-well plate, washed with 1x PBS, fixed with 4% paraformaldehyde (PFA) for 10 min, washed twice with 1x PBS, and stored in 0.1% PBS-azide at 4°C.

Immunofluorescence staining – Fixed hemocytes on coverslips were washed three times with 1x PBS (3 min, shaking) and incubated for 1 h at room temperature (RT) under shaking in blocking buffer: 0.2% Triton X-100 (DAKO, Glostrup, Denmark), 0.3% Tween-20 (Sigma-Aldrich, St. Louis, USA), 5% bovine serum albumin (BSA, Sigma-Aldrich, St. Louis, USA), and 5% sucrose (VWR, Radnor, USA). Cells were stained with Alexa Fluor 647-phalloidin (1:400, Thermo Fisher Scientific, USA) in PBS for 1 h at RT while shaking. Hemocytes were then washed with 1x PBS (3 min, shaking), followed by DAPI-staining (1:10.000) for 15 min at RT while shaking. Following two 1x PBS washes (3 min, shaking) and a Milli-Q rinse, coverslips were mounted onto glass slides using fluoromount-G (Invitrogen, Carlsbad, USA). Slides were dried overnight and stored at 4°C.

D. melanogaster embryo isolation – Embryos were collected on apple juice agar plates supplemented with yeast paste. Following 24 h of acclimatization in laying cages at 25°C, agar plates were refreshed, and embryos were harvested after 20 h using cell strainers. Embryos were dechorionated in sodium hypochlorite for 2 min, washed 8 times with water, and stage 15 embryos were isolated. Selected embryos were immersed in Voltalef oil (VWR, Radnor, USA) and immobilized on double-sided tape between glass coverslips.

MACS primary microglia isolation – Brains from 21-day-old WT and *Disc1* LI mice were dissected in ice-cold HBSS (Gibco, Grand Island, USA) to remove the cerebellum, olfactory bulb, and meninges, and transferred to cold DMEM (1% P/S). Tissues were mechanically dissociated and enzymatically digested using 0.5 mM EDTA, 0.3 mg/ml DNase I (Roche, Mannheim, Germany), 3 mM L-cysteine (Sigma-Aldrich, Overijse, Belgium), and 25 U/ml papain (Sigma-Aldrich, St. Louis, USA) for 30 min at 37°C, while shortly mixing halfway through incubation. The suspension was filtered through a DMEM-prewashed 70 µm strainer, centrifuged at 500 G for 10 min at RT, and resuspended in a 30% Percoll gradient. A 70% Percoll layer was created underneath, cold 1x PBS was added on top, and the sample was centrifuged at 650 rpm for 25 min at RT (acceleration 4, brake 0). The myelin layer was aspirated, and the interface cell layer was collected, washed in 1x PBS, and centrifuged at 500 G for 5 min at 4°C. The pellet was resuspended in MACS buffer (0.5% FCS, 0.5% EDTA, and 99% 1x PBS) and incubated with CD11b beads (Miltenyi Biotec, Bergisch Gladbach, Germany) for 15 min at 4°C in the dark. Cells were resuspended in MACS buffer, centrifuged at 300 G for 10 min at 4°C, loaded onto LS columns (Miltenyi Biotec, Bergisch Gladbach, Germany) on a magnetic stand, and washed three times with MACS buffer to elute all $CD11b^-$ cells. Finally, columns were removed from the magnet to collect $CD11b^+$ microglia. Cells were centrifuged (300 G for 10 min at 4°C), resuspended in freezing medium (90% DMEM/FCS, 10% DMSO; PanReac Appli-Chem, Barcelona, Spain), and

cryopreserved at -80°C prior to liquid nitrogen storage.

Quantitative polymerase chain reaction (qPCR) – BV2 cells and primary microglia were lysed by Qiazol (Qiagen, Hilden, Germany) for 5 min at RT, and total RNA was isolated via chloroform-phase separation and the RNeasy Mini Kit (Qiagen) according to the manufacturer's protocol. The upper phase was transferred and mixed with 70% ethanol. This mixture was transferred to a RNeasy column and washed with buffers RW1 and RPE. RNA was eluted with RNase-free water, and concentration and purity were assessed using a Nanodrop ND-2000 spectrophotometer. RNA was stored at -20°C until needed for cDNA synthesis. cDNA was synthesized by mixing RNA (80%) with Qscript cDNA supermix (20%, Quanta Biosciences, Beverly, USA), using a T100™ thermal cycler (Biorad, Hercules, USA) with the following parameters: 5 min at 25°C, 30 min at 42°C, and 5 min at 85°C. qPCR was performed on a QuantStudio3 (Applied Biosystems, Foster City, USA) using a master mix containing 67% SYBR Green (Applied Biosystems, Foster City, USA), 25% Milli-Q, and 4% of each forward/reverse primer. RNase-free water was used as a negative control. Cycling parameters were set at a hold stage of 1x 20 seconds (s) at 95°C, a PCR stage of 40x 1s at 95°C followed by 20s at 60°C, and a melt curve stage of 1x 1s at 95°C, 20s at 60°C, and 1s at 95°C. Primer efficiencies were calculated via logarithmic cDNA dilutions. Target gene (*Fchsd2* and *Diaph2*) expression was normalized to reference genes *Rpl13a* and *Hprt1* (Supplementary table 1).

Confocal microscopy and image acquisition – Following immunofluorescent staining, *Drosophila* hemocytes were imaged using a Zeiss LSM 900 confocal microscope equipped with a 63x (NA 1.4) oil objective. Lasers were set at 640 nm, and cells were imaged with 19 Z-stacks having 0.19 µm intervals. For quantitative analysis, Fiji software was used to define cell area and perimeter by manual thresholding. The cell circularity was calculated using equation (1). A value of 1 indicates a perfect circle. The segmented line tool was used to measure the number and length of individual filopodia per cell. Only filopodia longer than 1 µm were included in the analysis. For *in vivo* embryo imaging, acquisition was performed with a Zeiss LSM 880 confocal microscope equipped with an AiryScan detector for LifeAct-GFP images and a 40x water-immersion objective. An argon laser was set to 488 nm and 594 nm, and cells were imaged with 12 Z-stacks at 1 µm intervals. For quantitative analysis, the TrackMate plugin in Fiji was applied to obtain migratory parameters, including track displacement, directionality, and mean speed.

$$Cell\ circularity = 4\pi\ x\ \frac{Area}{Perimeter^2} \quad (1)$$

Statistical analysis – All analyses were performed using GraphPad Prism 10. A Shapiro-Wilk test was applied to assess normality, followed by the appropriate statistical test. For multi-group hemocyte morphology parameters and *in vivo* migration, statistical differences were determined using a Welch ANOVA test followed by a Dunnett's T3 multiple comparison test or a nonparametric Kruskal-Wallis test followed by Dunn's multiple-comparison post hoc test. For qPCR expression profiles, comparisons were performed using a Welch's test. A p-value < 0.05 was used as a threshold for statistical significance.

RESULTS

dia and nwk oppositely regulate hemocyte morphology – To evaluate the roles of *dia* and *nwk* in actin cytoskeletal organization, the hemocyte-specific srp.hemo-GAL4 driver expressed RNAi constructs of *dia* and *nwk* in *D. melanogaster*. Following isolation and phalloidin staining of these hemocytes, it was shown that knockdown of the formin-related gene *dia* (srp.hemo-GAL4 > GFP, RNAi-*dia*) produced significantly larger, rounder cells, whereas depletion of the Arp2/3 regulator *nwk* (srp.hemo-GAL4 > GFP, RNAi-*nwk*) shifted the cellular equilibrium toward a highly irregular morphology (Figure 1a). The *dia*-depleted hemocytes showed increased cell area (261.982 µm^2) compared to both Yv^1 (negative) (137.832 µm^2) and *scar* (positive) (180.082 µm^2) controls, and significantly higher cell circularity (0.515) than the *scar* knockdowns (0.250) (Figure 1b, c). Conversely, the *nwk*-depleted cells exhibited a significantly larger area (183.145 µm^2) than the *scar* control. Their circularity (0.349) was significantly reduced compared to both the Yv^1 controls (0.478) and the *dia*-depleted cells (Figure 1b, c). To confirm that these distinct morphological alterations

were strictly driven by GAL4-mediated knockdown, rather than genetic background leakage of the transgene, driverless controls (UAS-RNAi) were evaluated (Supplementary figure 1). These driverless control lines retained a cell circularity comparable to the baseline Yv^1 control. A clear significant difference in cell circularity was observed between the *scar* (0.451) and *nwk* (0.474) driverless controls and their functional knockdowns. For *dia* (0.434), no significant difference in cell circularity was observed. Taken together, these results indicate that *dia* and *nwk* exert opposing regulatory effects on cell morphology, with *dia* knockdown driving a spread, circular phenotype, and *nwk* depletion driving an asymmetrical, irregularly shaped morphology.

dia and nwk oppositely regulate filopodia formation – To further evaluate the effect of these targeted knockdowns on the lamellipodia-filopodia balance, the protrusions were quantified in the phalloidin-stained hemocytes. *dia*-depleted hemocytes exhibited a significant reduction in average filopodia number (1.402) compared to the *scar* control (11.988), though they did not differ significantly from Yv^1 (1.579) (Figure 1a, d). In contrast, *nwk* knockdown resulted in a significant increase in filopodia number (6.645) compared to Yv^1 hemocytes, though this count remained significantly lower than in *scar* hemocytes. A direct comparison of the two experimental groups showed that *nwk*-depleted hemocytes had significantly more filopodia than *dia*-depleted hemocytes. Notably, no significant differences were observed in the mean lengths of filopodia between any of the target genes or control groups (Yv^1 = 2.076 µm, *scar* = 2.104 µm, *nwk* = 2.144 µm, *dia* = 2.370 µm) (Figure 1a, e). These results indicate that RNAi-mediated knockdown of *dia* suppresses filopodia formation, whereas knockdown of the opposite side of the equilibrium (*nwk*) promotes a filopodia-dominant cellular architecture.

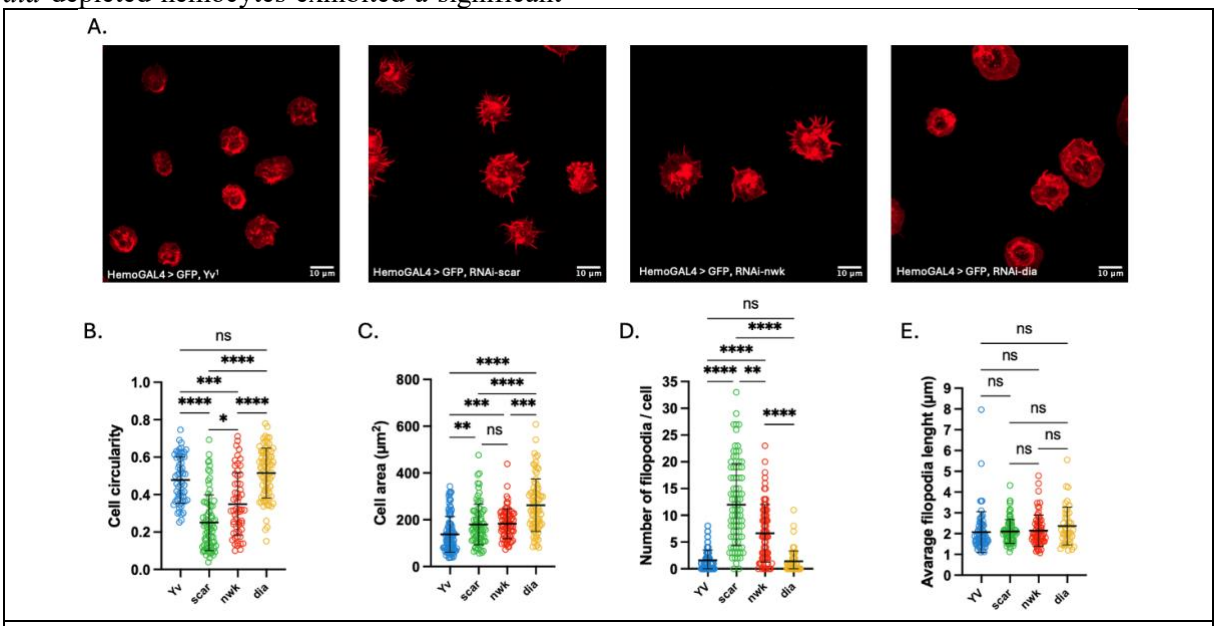

Figure 1: *dia* and *nwk* oppositely regulate hemocyte morphology. *Drosophila melanogaster* strains were crossed to obtain hemocytes containing the genotype HemoGAL4 > GFP, Yv1 (negative control), HemoGAL4 > GFP, RNAi-*scar* (positive control), HemoGAL4 > GFP, RNAi-*dia*, HemoGAL4 > GFP, RNAi-*nwk*. (**A**) Confocal microscopy images of primary hemocytes, isolated from *Drosophila melanogaster* third-instar larvae. Filamentous actin was visualized using phalloidin-647 iFluor staining (red). Imaging was performed using a Zeiss LSM 900 confocal microscope, and analysis was performed using Fiji. Scale bar represents 10 µm. (**B**) Quantification of cell circularity (0 = irregular, 1 = perfect circle) and (**C**) cell area (µm²). (**D**) Analysis of the number of filopodia per cell and (**E**) the mean filopodial length (µm). Data represent mean ± SD from six independent experiments (n = 105 Yv^1, n = 77 *scar*, n = 56 *nwk*, n = 81 *dia*). ****P < 0.0001, ***P < 0.001, **P < 0.01, *P < 0.05, Kruskal-Wallis test followed by Dunn's multiple comparisons test. *dia*, diaphanous; hemo, hemocyte; ns, not significant; *nwk*, nervous wreck; *scar*, suppressor of cAMP receptor; Yv^1, yellow vermillion.

dia and nwk do not influence hemocyte morphology in vivo – To evaluate the *in vivo* roles of *dia* and *nwk* on actin cytoskeletal organization, the srp.hemo-GAL4 driver co-expressed UAS-LifeAct-GFP alongside the UAS-RNAi constructs of *dia* and *nwk.* Following embryo isolation, live-cell imaging revealed that all conditions showed actin-rich structures (Figure 2). Qualitatively, the overall cellular morphology appeared broadly comparable between the conditions, with prominent protrusions consistently present across all evaluated genotypes. Visually, Yv^1 control embryos displayed a high density of hemocytes tightly organized into three distinct migratory strands spanning along VNC. In contrast, this stereotypical spatial distribution appeared less defined in *scar*-depleted embryos, where hemocytes exhibited a more disorganized arrangement. In the *nwk* knockdown, hemocytes appeared more heterogeneous with irregular morphologies compared to the other conditions. The *dia*-depleted hemocytes appeared to be less directionally elongated. Taken together, these results indicate that knockdown of *dia* and *nwk* does not visibly disrupt hemocyte morphology or actin organization *in vivo*, leaving no distinguishable phenotypes.

dia and nwk oppositely regulate in vivo hemocyte migration dynamics – To determine the roles of *dia* and *nwk* in hemocyte migration *in vivo*, live time-lapse imaging was performed on stage 15 *D. melanogaster* embryos expressing hemocyte-specific H2ACherry. Automated tracking analysis of hemocyte trajectories revealed distinct visual variations in migration patterns between *LexA* (scramble control), *dia*, and *nwk* knockdown embryos (Figure 3a, b). In *nwk*-depleted embryos, a visibly lower density of tracks was observed, and the persisting trajectories appeared shorter and less widely dispersed throughout the embryo compared to the other genotypes. Quantitative characterization of the migratory parameters demonstrated that knockdown of *dia* led to a significant increase in total traveled distance (69.147 µm) compared to both the *LexA* control (51.407 µm) and *nwk* knockdown (47.596 µm). Interestingly, this kinetic enhancement did not translate into an increase in net displacement, as no statistically significant differences in total track displacement were observed among the *LexA* (12.642 µm), *nwk* (12.113 µm), and *dia* (10.529 µm) groups (Figure 3c). For migration velocity, a significant reduction in mean migration speed was observed in *nwk*-depleted hemocytes (0.0297 µm/s) compared to the *LexA* control (0.0385 µm/s), whereas *dia* knockdown significantly elevated mean speed above all tested genotypes (0.0497 µm/s).

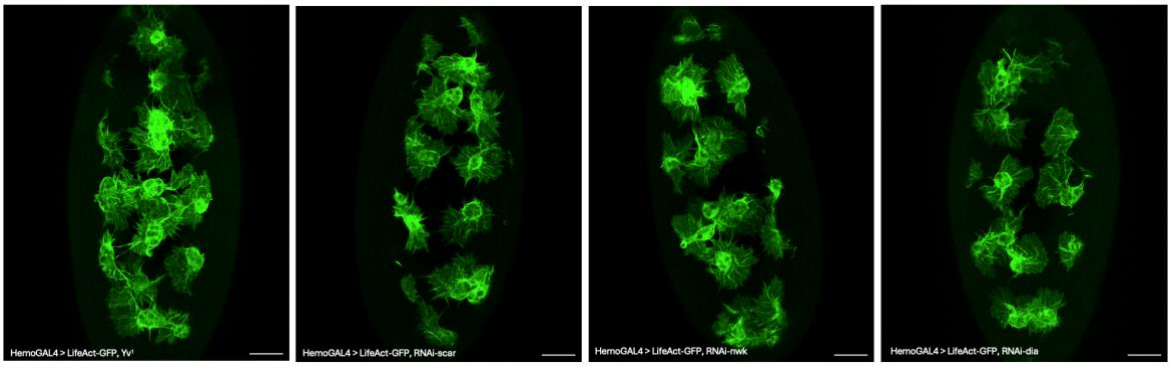

Figure 2: *dia* and *nwk* do not influence hemocyte morphology *in vivo*. Confocal microscopy images showing the hemocyte actin cytoskeleton in stage 15 *Drosophila melanogaster* embryos. The actin cytoskeleton is visualized using a HemoGAL4-driven LifeAct-GFP construct (green). *Drosophila melanogaster* strains were crossed to obtain embryos containing hemocytes with the genotype HemoGAL4 > LifeAct-GFP, Yv^1 (negative control), HemoGAL4 > LifeAct-GFP, RNAi-*scar* (positive control), HemoGAL4 > LifeAct-GFP, RNAi-*nwk* (target gene), HemoGAL4 > LifeAct-GFP, RNAi-*dia* (target gene). Imaging was performed using a Zeiss LSM 880 confocal microscope, and analysis was performed using Fiji. Scale bar represents 20 µm. *dia*, diaphanous; hemo, hemocyte; *nwk*, nervous wreck; *scar*, suppressor of cAMP receptor; Yv^1, yellow vermillion.

This variation was strictly confined to baseline motility, as the mean straight-line speed did not differ significantly among the groups (*LexA* = 0.0103 µm/s, *nwk* = 0.00800 µm/s, *dia* = 0.00894 µm/s) (Figure 3d). Regarding parameters for directionality, no significant differences in the confinement ratio were observed among *LexA* (0.261), *dia* (0.181), and *nwk* (0.278). However, the mean directional change rate was significantly higher in both *nwk* (0.0407 rad/s) and *dia* (0.0440 rad/s) depleted embryos compared to the negative control (0.0361 rad/s) (Figure 3e). Overall, these data indicate that knockdown of *dia* and *nwk* alters specific quantified parameters of *in vivo* hemocyte migration, namely total distance, mean speed, and directional change rate.

qPCR primers revealed target-specific amplification in BV2 cells and primary murine microglia – To successfully perform qPCR, transcript-specific primers were designed (Supplementary table 1). Initial optimization and validation were performed using the BV2 microglial cell line. The primer sets used for the housekeeping genes *Rpl13a* and *Hprt1* exhibited efficiencies of 129.725% and 119.953%, respectively.

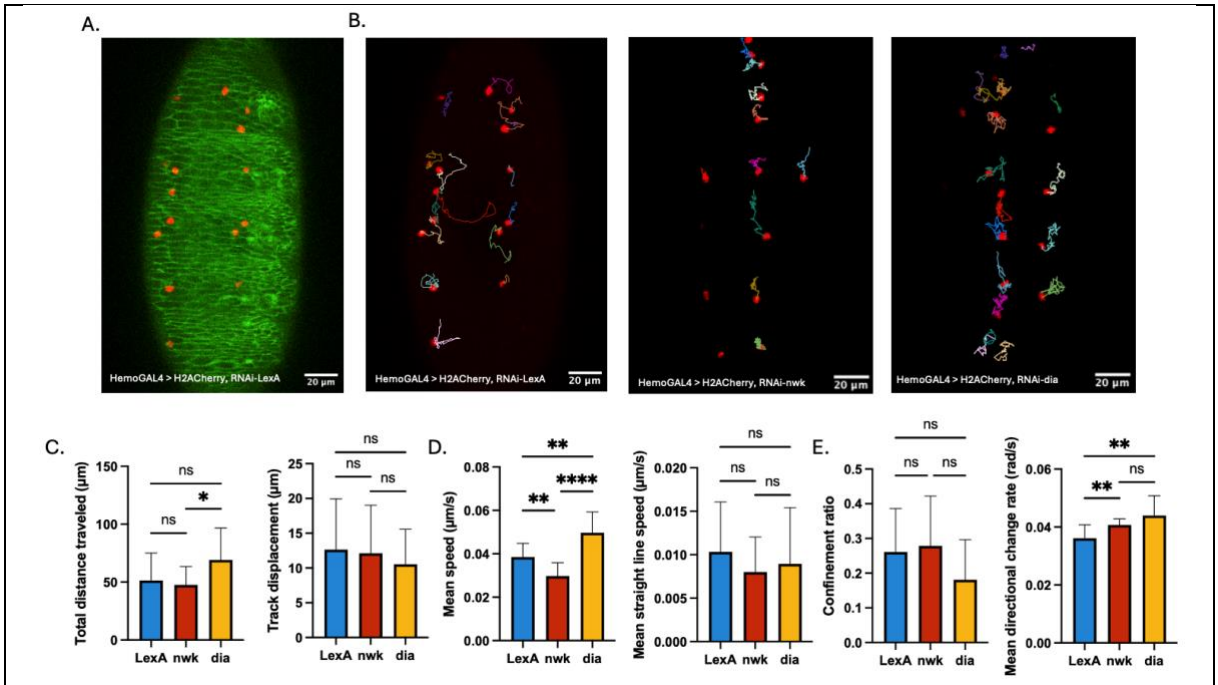

Figure 3: *dia* and *nwk* oppositely regulate *in vivo* hemocyte migration dynamics. *Drosophila melanogaster* strains were crossed to generate embryos containing hemocytes with genotypes HemoGAL4 > H2ACherry, RNAi-*LexA* (negative control), HemoGAL4 > H2ACherry, RNAi-*dia*, and HemoGAL4 > H2ACherry, RNAi-*nwk*. (**A**) Representative confocal images of hemocyte nuclei and epithelium in stage 15 *Drosophila melanogaster* embryos, visualized using the NRG and H2ACherry reporter. (**B**) Hemocyte migration tracks were generated from live time-lapse imaging over 30 min (61 frames, 30 s intervals). Only tracks with a minimum duration of > 10 frames (> 300 s) were included in the analysis. Each color represents an individual cell track. Time-lapse imaging was performed using a Zeiss LSM 880 confocal microscope, and track analysis was performed using TrackMate in Fiji. Scale bar represents 20 µm. (**C**) Quantification of overall hemocyte motility, including total distance traveled (cumulative path length) and track displacement (net distance between track start and endpoint). (**D**) Quantification of migration velocity, including mean speed and mean straight-line speed. (**E**) Quantification of migration directionality and persistence, including confinement ratio and the mean directional change rate. Quantification was performed on migration tracks derived from one representitive embryo per genotype (n = 1). Data repressents mean ± SD. Statistical significance was assesed using the Welch ANOVA test followed by Dunnett's T3 multiple comparisons test or Kruskal-Wallis test followed by Dunn's multiple comparisons test. *dia*, diaphanous; hemo, hemocyte; H2A, Histone 2A; *LexA*, Locus for Expression of SOS Genes A; ns, not significant; *nwk*, nervous wreck.

The primer efficiencies for *Fchsd2* and *Diaph2* were 153.071% and 362.358% (Supplementary figure 2a, Supplementary table 2). Melt curve analysis of both the reference genes (*Rpl13a* and *Hprt1*) and the target genes (*Fchsd2* and *Diaph2*) showed single, distinct peaks (Supplementary figure 2b). A similar validation experiment was performed in primary murine microglia. Here, the primer sets exhibited efficiencies of 96.496% for *Rpl13a* and 99.826% for *Hprt1*. The primer efficiencies for *Fchsd2* and *Diaph2* were 158.759% and 140.247% (Figure 4a) (Table 1). Melt curve analysis of the primer sets for all genes showed single, distinct peaks (Figure 4b). Taken together, the successful validation and single-peak melt curves demonstrate that the designed primer sets are highly target-specific and suitable for robust relative quantification.

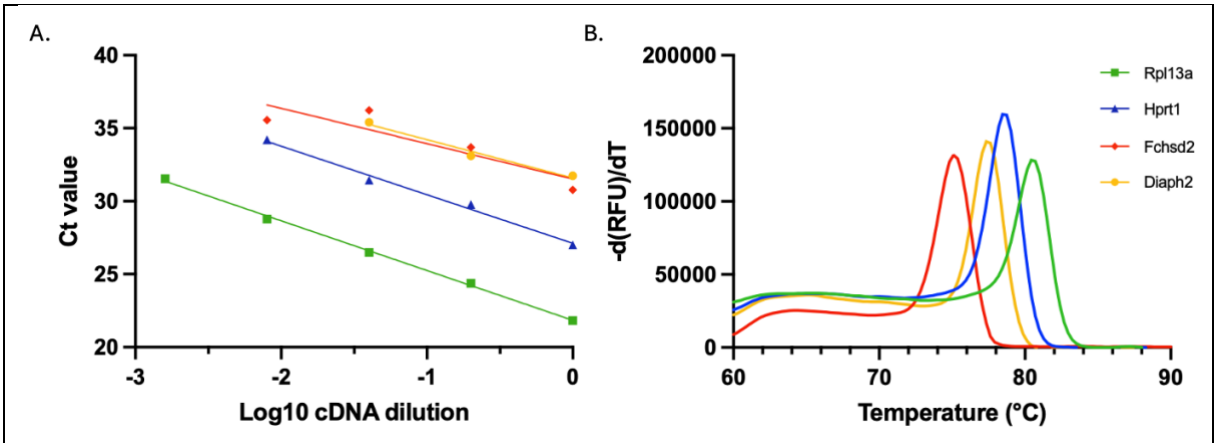

Figure 4: qPCR primers showed target-specific amplification in primary murine microglia. (**A**) Standard curve analysis for two reference genes (*Rpl13a*, *Hprt1*) and two target genes (*Fchsd2*, *Diaph2*). Cycle threshold values are plotted against log10-transformed relative cDNA dilution factors derived from a 5-fold serial dilution series of pooled primary microglia cDNA (undiluted, 1/5, 1/25, 1/125, 1/625). Each data point (square, triangle, circle, diamond) represents a single reaction. Linear regression lines are colored according to the legend, each representing a single gene. (**B**) Melt curve analysis showing the negative derivative of fluorescence over temperature, plotted against the melting temperature (°C), for each primer set, with single measurements shown. cDNA, complementary DNA; ct, cycle treshold; *Diaph2*, diaphanous related-formin 2; *Fchsd2*, FCH and double SH3 domain 2; *Hprt1*, hypoxanthine phosphoribosyltransferase 1; RFU, relative fluorescent units; *Rpl13a*, Ribosomal protein L13a.

Table 1: Amplification efficiencies and standard curve metrics of qPCR primers in primary murine microglia. Parameters, including the slope, coefficient of determination (R^2), and calculated primer efficiency (%) derived from a 5-fold dilution standard curve, are represented for the reference genes (*Rpl13a*, *Hprt1*) and target genes (*Fchsd2*, *Diaph2*).

	Slope	R^2	Primer efficiency (%)
Rpl13a	-3.409	0.998	96.496
Hprt1	-3.326	0.991	99.826
Fchsd2	-2.422	0.798	158.759
Diaph2	-2.627	0.979	140.247

Diaph2, diaphanous related-formin 2; *Fchsd2*, FCH and double SH3 domain 2; *Hprt1*, hypoxanthine phosphoribosyltransferase 1; *Rpl13a*, Ribosomal protein L13a.

Fchsd2 and Diaph2 show no significant differential expression in WT and Disc1 LI primary murine microglia – To validate the distinct expression profile of *Fchsd2* and *Diaph2* observed in *Disc1* LI murine microglia using scRNA-seq, qPCR analysis was performed. Both *Fchsd2* and *Diaph2* exhibited high threshold cycle (Ct) values across both WT and *Disc1* LI primary microglia (Figure 4a). These Ct values were normal for the respective housekeeping genes. Regarding relative expression levels, a quantification was performed with the WT baseline set at 1. This analysis indicated no significant differences in transcript levels compared to *Disc1* LI microglia, yielding mean fold changes of 1.069 for *Fchsd2* and 1.748 for *Diaph2* (Figure 5). These findings indicate that *Diaph2* and *Fchsd2* are not robustly altered in *Disc1* LI microglia, meaning that the preliminary scRNA-seq data could not be validated using qPCR.

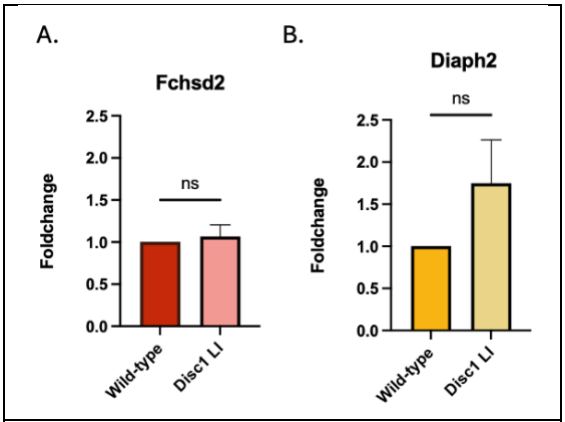

Figure 5: *Fchsd2* and *Diaph2* show no significant differential expression in WT and *Disc1* LI primary murine microglia. Relative expression levels of (**A**) *Fchsd2* and (**B**) *Diaph2* in primary microglia, isolated from 21-day-old WT and *Disc1* LI mice. Values represent the mean fold change calculated via the $2^{-\Delta\Delta Ct}$ method, normalized against *Rpl13a* and *Hprt1* housekeeping genes. The WT expression level serves as the baseline reference (set at 1.0). Data represent the mean ± SD of three pooled biological replicates. Statistical significance was assesed using the Welch's test. *Diaph2*, diaphanous related-formin 2; *Disc1*, Disrupted-in-Schizophrenia 1; *Fchsd2*, FCH and double SH3 domain 2, LI, Locus Impairment; ns, not significant.

DISCUSSION

The aim of this study was to elucidate how the actin regulators *dia* and *nwk* modulate the phagocytic cytoskeleton, and to determine how these molecular mechanisms dictate hemocyte morphology and motility. To achieve this objective, an RNAi-mediated knockdown strategy targeting *dia* and *nwk* was deployed in *D. melanogaster.*

Under *in vitro* conditions, *dia*-deficient hemocytes exhibited a marked increase in both cell circularity and total cell area, accompanied by a prominent collapse of filopodia relative to the control groups (Figure 1a-e). These findings underscore a direct role for *dia* in modulating the homeostatic equilibrium between formins and the Arp2/3 complex, thereby dictating cellular architecture. These results are consistent with several prior independent studies. First, overexpression of $dia^{\Delta DAD}$ in hemocytes yielded a filopodia-dominant morphology, corroborating the instructive role of *dia* activity levels in shaping hemocyte architecture (36). Second, endogenous depletion of *dia* in *D. melanogaster* epidermal cells has previously been shown to induce a lamellipodia-dominant morphology, whereas overexpression resulted in the opposite, filopodia-dominant phenotype (37). Third, analogous morphological shifts have been reported in amoeba *in vitro*, where overexpression of *dia* drove filopodia dominance and complete loss-of-function mutations produced lamellipodia dominance (38). At the molecular level, as a member of the formin family, *dia* (ortholog to the mammalian DIAPH2) nucleates linear actin filaments. Depletion of *dia* disrupts actin monomer homeostasis, shifting the polymerizing machinery toward Arp2/3-dominant branched actin networks. This unconstrained branched polymerization drives the plasma membrane outward, generating expansive lamellipodia that significantly increase the overall cell surface area (39,40). Furthermore, the loss of linear actin architecture compromises the formation of contractile stress fibers and filopodial precursors. Because these linear structures are essential for generating intracellular tension, establishing a migratory axis, and extending protrusions, *dia* knockdown ultimately resulted in the observed phenotype (16,41).

Conversely, *nwk*-depleted hemocytes adopted a more irregular, less circular morphology, characterized by an elevated

number of filopodia, compared to the Yv^1 negative control (Figure 1a-e). To our knowledge, no prior study has directly examined the effect of *nwk* depletion on hemocyte morphology, making this a novel finding. Nevertheless, indirect support comes from several studies. One demonstrated that *nwk* plays a role in membrane morphology beyond its canonical endosomal function. More specifically, the *nwk* F-BAR domain can induce membrane deformations through actin filament assembly (42,43). Further corroboration comes from studies on the mammalian ortholog FCHSD2. Here, despite activating Arp2/3, the protein promotes protrusion formation by acting locally within nascent protrusions rather than globally across the membrane (44). Knockdown of nwk/FCHSD2 consequently reduces this localized Arp2/3 complex activation, freeing actin monomers for formin-driven filopodia formation (45). This is directly consistent with the phenotype observed in this study. The intermediate severity of the *nwk* knockdown phenotype reflects these mechanistic distinctions. Unlike *scar*/WAVE, which directly and globally drives Arp2/3 activation at the plasma membrane, *nwk* acts more indirectly through upstream activation of WASp (21,45,46). As a result, it primarily coordinates localized Arp2/3 activity during endosomal constriction and vesicle trafficking. This distinct cellular role accounts for the more nuanced morphological alterations observed following *nwk* depletion, in contrast to the global architectural collapse triggered by *scar* depletion.

Following the characterization of *dia* and *nwk in vitro*, the transgenic marker LifeAct-GFP was utilized to evaluate their roles *in vivo*. LifeAct-GFP enables the direct visualization of filamentous actin dynamics in living cells, thereby providing substantially more structural resolution regarding hemocyte morphology than standard cytosolic GFP (Supplementary figure 3) (47). In contrast to the pronounced *in vitro* defects, live-cell imaging of the embryo revealed that all conditions exhibited clear cell-surface protrusions, and no distinct morphological phenotypes could be distinguished following the knockdown of *dia* or *nwk* (Figure 2). Notably, as previously described, a prior study demonstrated that overexpression of $dia^{\Delta DAD}$ in hemocytes produced a clearly filopodia-dominant morphology when visualized *in vivo* using LifeAct-GFP (36). This therefore suggests that the *in vivo* actin machinery is responsive to sufficiently strong perturbations of *dia* activity. The absence of a comparable phenotype under knockdown conditions in the present study may therefore reflect that partial loss of *dia* function falls below the threshold required to override the buffering capacity of the *in vivo* microenvironment. This contrast highlights the complexity of translating isolated cellular behaviors to an *in vivo* setting. Within the developing embryo, hemocytes are exposed to various overlapping microenvironmental cues. Throughout this developmental stage, these cells must simultaneously coordinate polarization, interstitial migration, and the phagocytosis of apoptotic debris, processes that continually redirect and reorganize the actin cytoskeleton (48). This constant developmental polarization and functional multitasking may mask or suppress the distinct filopodial or lamellipodial phenotypes observed *in vitro.* Conversely, analyzing hemocytes *in vitro* on rigid glass coverslips eliminates these confounding tissue-level variables. Upon contact with the glass, the cells adapt to an isotropic substrate, lose their native developmental polarization axes, and adopt a highly attached morphology (49). Beyond individual cell morphology, the global spatial distribution of hemocytes throughout the embryo can also be influenced by disruptions in actin regulators. For instance, Yv^1 control embryos displayed a high density of hemocytes tightly organized into three distinct migratory strands spanning along the VNC. In contrast, this stereotypical spatial distribution appeared less defined in *scar*-depleted embryos, where hemocytes exhibited a more disorganized arrangement. This impaired distribution could stem either from defective cell motility driven by disrupted actin remodeling or from upregulation of phagocytic activity that prioritized debris clearance over directional migration.

Having established that *dia* and *nwk* regulate hemocyte cytoskeletal architecture, it was subsequently investigated whether these structural alterations extend to actin dynamics. This process directly governs multiple cell functions, including migration, a key hemocyte function required in normal neurodevelopment. This was therefore assessed through quantitative *in vivo* migration analysis. Tracking of hemocyte migration revealed that

dia-depleted hemocytes exhibited a significant increase in total traveled distance and mean migration speed compared to the *LexA* RNAi scramble control. Yet net displacement and mean straight-line speed remained unchanged (Figure 3a-e). This is consistent with prior studies showing that overexpression of *dia* in hemocytes reduced migration speed, and that null mutation of *dia* increased migration speed in amoeba (36,38). Together, these findings suggest that *dia*-depleted hemocytes move more extensively, but without directional persistence, as supported by the elevated mean directional change rate. This behavior is consistent with the collapse of filopodia observed *in vitro*: without filopodia to sense environmental cues, chemotactic guidance is impaired, and movement becomes random. The broad lamellipodia that replace filopodia likely reduce substrate anchoring, permitting faster, but undirected displacement (50,51). In contrast, *nwk*-depleted hemocytes showed a significantly reduced mean migration speed compared to both *dia*-depleted and control hemocytes, alongside an elevated directional change rate (Figure 3a-e). This aligns with a prior study showing that inhibition of FCHSD2 reduced migration in mammalian cancer cells (52). The combination of low speed and high directional change rate suggests that the filopodia-dominant morphology causes cells to continuously probe their surroundings while remaining largely anchored, resulting in slow, highly exploratory, yet spatially confined movement (50,51). Collectively, these migratory profiles directly reflect the cytoskeletal architectures identified *in vitro*, demonstrating that the lamellipodia-filopodia balance governed by *dia* and *nwk* has tangible consequences for hemocyte motility *in vivo*.

To investigate whether the cytoskeletal regulatory frameworks governed by *dia* and *nwk* extend to mammalian microglia, this study transitioned toward verifying the downregulation of *Diaph2* and *Fchsd2* in *Disc1* LI microglia via qPCR. To achieve this, initial primer validation was conducted using the murine BV2 microglial cell line, which provides an abundant, cost-effective, and easily maintainable source of cellular material (53). Using this cell line established an ideal screening platform to rapidly evaluate multiple primer designs before performing experiments on the scarce pool of primary murine microglia (Supplementary figure 2, Supplementary table 2). qPCR analysis confirmed that the primer design for the reference genes *Rpl13a* and *Hprt1* was highly suitable, demonstrating target-specific amplification and optimal amplification efficiencies (Table 1) (Figure 4a, b). These values fall perfectly within the universally accepted standard efficiency range of 90-110% (54). Conversely, while *Diaph2* and *Fchsd2* also exhibited target-specific amplification, their calculated efficiencies fell substantially outside the standard range. These anomalously high efficiency values are a documented mathematical artifact arising when analyzing low-abundance transcripts with high baseline Ct values. Because *Diaph2* and *Fchsd2* are weakly expressed in microglial cells, the highly diluted samples in the serial dilution series (up to 1/625) approach or fall below the assay's lower limit of quantification. At these detection limits, stochastic amplification failure and background noise disrupt the linearity of the standard curve. This flattening of the standard curve slope artificially inflates the calculated efficiency percentage. Given these constraints on standard curve linearity, primer validation relied primarily on melting curve profiles, which showed clean single peaks, indicating absolute target specificity without primer-dimer formation. Consequently, the primer sets for *Rpl13a*, *Hprt1*, *Diaph2*, and *Fchsd2* were deemed specific and technically viable for subsequent gene expression profiling.

qPCR analysis revealed no statistically significant differences in the transcript expression levels of *Diaph2* and *Fchsd2* between WT and *Disc1* LI primary microglia (Figure 5). This outcome does not corroborate and therefore fails to validate the preliminary scRNA-seq dataset that originally prompted this line of investigation. This transcriptomic analysis indicated downregulation of both genes. Several technical and biological factors likely account for this discrepancy. First, the preliminary scRNA-seq analysis was performed on untransformed, un-normalized raw count data, which increases susceptibility to false-positive differential expression artifacts. Second, both *Diaph2* and *Fchsd2* exhibited high baseline Ct values ($Ct > 30$), reflecting very low transcript abundance in primary murine microglia. At these high cycle numbers, qPCR amplification is heavily affected by noise, which dramatically inflates variance across biological and technical replicates. Because the true expression difference between WT and

Disc1 LI conditions may be subtle, a baseline fluctuation of 1-2 Ct values driven solely by technical noise can entirely mask genuine biological differences (55). A direct solution to resolve this detection threshold issue would be to increase the starting cDNA concentration. However, our primary cell isolation protocol yielded approximately 150,000 primary microglia per mouse brain, resulting in low total RNA concentrations ranging from 10-20 ng/µl. To scale up cDNA synthesis sufficiently to overcome the detection limits of these low-abundance targets, future experiments would require the pooling of a significantly larger number of murine brains than was logistically feasible in this project. Alternatively, shifting the validation strategy from transcript-level qPCR to protein-level immunocytochemistry (ICC) presents a highly viable alternative. Primary microglia could be incubated with target-specific antibodies for *Diaph2* and *Fchsd2*. Quantifying relative protein abundance by measuring single-cell mean fluorescence intensity differences between WT and *Disc1* LI microglia would provide a sensitive alternative assay. By evaluating the translated protein product directly, this approach circumvents the stochastic limitations of low-copy-number nucleotide amplification, potentially offering a more robust validation of the expression trends flagged by scRNA-seq (56).

Several technical and experimental limitations must be considered when interpreting the findings of this study. Regarding the *in vitro* hemocyte morphological quantifications, cell area and circularity were determined using manual thresholding protocols in Fiji, which introduces the possibility of minor investigator bias. Additionally, the mean filopodia length showed no significant difference, as averaging measurements across such a large cell population can even out subtle variations. A major limitation of *in vivo* hemocyte morphology analysis compared to the *in vitro* setup was the absence of quantitative measurements. The complex embryo environment made thresholding more difficult, and the limited number of experimental repeats due to the optimization of these embryo protocols restricted the detection of differences in cell size, filopodia, or phagosome counts that were not visibly apparent. Similarly, the migration-tracking analysis was based on a single embryo per genotype (n = 1), severely limiting statistical power and making it difficult to draw definitive conclusions about the specific contributions of *dia* and *nwk* to hemocyte motility. Finally, due to low expression levels of *Diaph2* and *Fchsd2* in primary murine microglia, qPCR was unsuitable for validating subtle gene expression changes observed between WT and *Disc1* LI microglia.

To address these limitations, future research should focus on refining the *in vivo* embryo assays and increasing biological replication across the current platforms. Expanding these frameworks will facilitate the evaluation of more complex physiological behaviors linked to *dia* and *nwk,* including cellular surveillance and phagocytosis. Concurrently, the transcriptomic alterations identified by scRNA-seq must be validated using alternative, highly sensitive techniques, such as ICC. Following this cellular validation, the research should transition to a translational model. Building on the comprehensive analysis of *dia* and *nwk* in *D. melanogaster,* initial studies should evaluate whether overexpression of *Diaph2* and *Fchsd2* can rescue microglial phenotypes in murine microglial cell lines or primary cell cultures. Demonstrating such a functional rescue *in vitro* is an essential prerequisite before transitioning to an *in vivo* mammalian context. Ultimately, if these cellular models prove successful, subsequent translational research could investigate whether lentiviral-mediated overexpression of *Diaph2* and *Fchsd2* can alleviate the excessive synaptic pruning and cognitive deficits observed in the *Disc1* LI mouse model (10).

CONCLUSION

This study aimed to dissect the roles of the evolutionarily conserved actin regulators *dia* and *nwk* in modulating phagocyte structural dynamics, establishing a comparative framework between *D. melanogaster* hemocytes and mammalian microglia. Our primary results demonstrate that *in vitro* knockdown of the formin-related gene *dia* significantly increases cell area and circularity while collapsing filopodia, whereas depletion of *nwk* promotes an asymmetrical morphology with an elevated number of filopodia. This confirms that these genes uniquely balance formin-driven linear elongation and Arp2/3-mediated branched actin networks. *In vivo* embryo imaging revealed no distinct

morphological phenotypes, highlighting the regulatory complexity introduced by overlapping tissue-level environmental cues during embryogenesis. However, quantitative migration analysis demonstrated that these cytoskeletal alterations do extend to actin dynamics and cell function *in vivo*. *dia*-depleted hemocytes exhibited faster but directionally deficient movement, consistent with the loss of filopodia-mediated environmental sensing. In contrast, *nwk*-depleted hemocytes showed reduced speed alongside increased directional change rate, reflecting the spatially confined exploratory behavior associated with filopodia dominance. Together, these migratory profiles directly corroborate the cytoskeletal architectures identified *in vitro*. Furthermore, shifting to a mammalian model to validate *Disc1* LI transcriptomic data revealed critical technical bottlenecks, demonstrating that qPCR is an unsuitable framework for low-abundance transcripts such as *Diaph2* and *Fchsd2*. This technical bottleneck underscores the need to adopt high-sensitivity, single-cell protein-level validation methods, such as ICC, in future investigations. Ultimately, bridging these fundamental mechanisms from *D. melanogaster* to a mammalian context lays a crucial foundation for translational research, and targeting *Diaph2* and *Fchsd2* signaling pathways may offer a viable therapeutic avenue to rescue the aberrant synaptic pruning and cognitive deficits characteristic of the *Disc1* LI model and NDDs.

REFERENCES

1. Stiles J, Jernigan TL. The basics of brain development. Neuropsychol Rev. 2010 Dec;20(4):327–48. doi:10.1007/s11065-010-9148-4 PubMed PMID: 21042938; PubMed Central PMCID: PMC2989000.
2. Silbereis JC, Pochareddy S, Zhu Y, Li M, Sestan N. The Cellular and Molecular Landscapes of the Developing Human Central Nervous System. Neuron. 2016 Jan 20;89(2):248–68. doi:10.1016/j.neuron.2015.12.008 PubMed PMID: 26796689; PubMed Central PMCID: PMC4959909.
3. Südhof TC. Towards an Understanding of Synapse Formation. Neuron. 2018 Oct 24;100(2):276–93. doi:10.1016/j.neuron.2018.09.040 PubMed PMID: 30359597; PubMed Central PMCID: PMC6226307.
4. Schafer DP, Lehrman EK, Kautzman AG, Koyama R, Mardinly AR, Yamasaki R, et al. Microglia sculpt postnatal neural circuits in an activity and complement-dependent manner. Neuron. 2012 May 24;74(4):691–705. doi:10.1016/j.neuron.2012.03.026 PubMed PMID: 22632727; PubMed Central PMCID: PMC3528177.
5. Paolicelli RC, Bolasco G, Pagani F, Maggi L, Scianni M, Panzanelli P, et al. Synaptic pruning by microglia is necessary for normal brain development. Science. 2011 Sep 9;333(6048):1456–8. doi:10.1126/science.1202529 PubMed PMID: 21778362.
6. Kahn RS, Sommer IE, Murray RM, Meyer-Lindenberg A, Weinberger DR, Cannon TD, et al. Schizophrenia. Nat Rev Dis Primers. 2015 Nov 12;1:15067. doi:10.1038/nrdp.2015.67 PubMed PMID: 27189524.
7. Goellner B, Aberle H. The synaptic cytoskeleton in development and disease. Dev Neurobiol. 2012 Jan;72(1):111–25. doi:10.1002/dneu.20892 PubMed PMID: 21509946.
8. Lasser M, Tiber J, Lowery LA. The Role of the Microtubule Cytoskeleton in Neurodevelopmental Disorders. Front Cell Neurosci. 2018;12:165. doi:10.3389/fncel.2018.00165 PubMed PMID: 29962938; PubMed Central PMCID: PMC6010848.
9. Jaglin XH, Chelly J. Tubulin-related cortical dysgeneses: microtubule dysfunction underlying neuronal migration defects. Trends Genet. 2009 Dec;25(12):555–66. doi:10.1016/j.tig.2009.10.003 PubMed PMID: 19864038.
10. Kessels S, Trippaers C, Mertens M, Hamad I, Rombaut B, Janssen A, et al. Cytoskeletal control in adult microglia is essential to restore neurodevelopmental synaptic and cognitive deficits. Sci Adv. 2025 Aug 29;11(35):eadw0128. doi:10.1126/sciadv.adw0128 PubMed PMID: 40880479; PubMed Central PMCID: PMC12396340.
11. Parkhurst CN, Yang G, Ninan I, Savas JN, Yates JR, Lafaille JJ, et al. Microglia promote learning-dependent synapse formation through brain-derived neurotrophic factor. Cell. 2013 Dec 19;155(7):1596–609.

doi:10.1016/j.cell.2013.11.030 PubMed PMID: 24360280; PubMed Central PMCID: PMC4033691.
12. Deivasigamani S, Miteva MT, Natale S, Gutierrez-Barragan D, Basilico B, Di Angelantonio S, et al. Microglia complement signaling promotes neuronal elimination and normal brain functional connectivity. Cereb Cortex. 2023 Sep 16;33(21):10750–60. doi:10.1093/cercor/bhad313 PubMed PMID: 37718159; PubMed Central PMCID: PMC10629900.
13. Nimmerjahn A, Kirchhoff F, Helmchen F. Resting microglial cells are highly dynamic surveillants of brain parenchyma in vivo. Science. 2005 May 27;308(5726):1314–8. doi:10.1126/science.1110647 PubMed PMID: 15831717.
14. Franco-Bocanegra DK, McAuley C, Nicoll JAR, Boche D. Molecular Mechanisms of Microglial Motility: Changes in Ageing and Alzheimer's Disease. Cells. 2019 Jun 25;8(6):639. doi:10.3390/cells8060639 PubMed PMID: 31242692; PubMed Central PMCID: PMC6627151.
15. Blanchoin L, Boujemaa-Paterski R, Sykes C, Plastino J. Actin dynamics, architecture, and mechanics in cell motility. Physiol Rev. 2014 Jan;94(1):235–63. doi:10.1152/physrev.00018.2013 PubMed PMID: 24382887.
16. Davidson AJ, Wood W. Unravelling the Actin Cytoskeleton: A New Competitive Edge? Trends Cell Biol. 2016 Aug;26(8):569–76. doi:10.1016/j.tcb.2016.04.001 PubMed PMID: 27133808; PubMed Central PMCID: PMC4961066.
17. Swanson JA. Shaping cups into phagosomes and macropinosomes. Nat Rev Mol Cell Biol. 2008 Aug;9(8):639–49. doi:10.1038/nrm2447 PubMed PMID: 18612320; PubMed Central PMCID: PMC2851551.
18. Pollard TD, Borisy GG. Cellular motility driven by assembly and disassembly of actin filaments. Cell. 2003 Feb 21;112(4):453–65. doi:10.1016/s0092-8674(03)00120-x PubMed PMID: 12600310.
19. Goley ED, Welch MD. The ARP2/3 complex: an actin nucleator comes of age. Nat Rev Mol Cell Biol. 2006 Oct;7(10):713–26. doi:10.1038/nrm2026 PubMed PMID: 16990851.
20. Ridley AJ. Rho GTPase signalling in cell migration. Curr Opin Cell Biol. 2015 Oct;36:103–12. doi:10.1016/j.ceb.2015.08.005 PubMed PMID: 26363959; PubMed Central PMCID: PMC4728192.
21. Takenawa T, Suetsugu S. The WASP-WAVE protein network: connecting the membrane to the cytoskeleton. Nat Rev Mol Cell Biol. 2007 Jan;8(1):37–48. doi:10.1038/nrm2069 PubMed PMID: 17183359.
22. Mattila PK, Lappalainen P. Filopodia: molecular architecture and cellular functions. Nat Rev Mol Cell Biol. 2008 Jun;9(6):446–54. doi:10.1038/nrm2406 PubMed PMID: 18464790.
23. Kovar DR. Molecular details of formin-mediated actin assembly. Curr Opin Cell Biol. 2006 Feb;18(1):11–7. doi:10.1016/j.ceb.2005.12.011 PubMed PMID: 16364624.
24. Goode BL, Eck MJ. Mechanism and function of formins in the control of actin assembly. Annu Rev Biochem. 2007;76:593–627. doi:10.1146/annurev.biochem.75.103004.142647 PubMed PMID: 17373907.
25. Hayashi-Takagi A, Takaki M, Graziane N, Seshadri S, Murdoch H, Dunlop AJ, et al. Disrupted-in-Schizophrenia 1 (DISC1) regulates spines of the glutamate synapse via Rac1. Nat Neurosci. 2010 Mar;13(3):327–32. doi:10.1038/nn.2487 PubMed PMID: 20139976; PubMed Central PMCID: PMC2846623.
26. Duan X, Chang JH, Ge S, Faulkner RL, Kim JY, Kitabatake Y, et al. Disrupted-In-Schizophrenia 1 regulates integration of newly generated neurons in the adult brain. Cell. 2007 Sep 21;130(6):1146–58. doi:10.1016/j.cell.2007.07.010 PubMed PMID: 17825401; PubMed Central PMCID: PMC2002573.
27. Schönichen A, Geyer M. Fifteen formins for an actin filament: a molecular view on the regulation of human formins. Biochim Biophys Acta. 2010 Feb;1803(2):152–63. doi:10.1016/j.bbamcr.2010.01.014 PubMed PMID: 20102729.
28. Chesarone MA, DuPage AG, Goode BL. Unleashing formins to remodel the actin and microtubule cytoskeletons. Nat Rev

Mol Cell Biol. 2010 Jan;11(1):62–74. doi:10.1038/nrm2816 PubMed PMID: 19997130.

29. Mellor H. The role of formins in filopodia formation. Biochim Biophys Acta. 2010 Feb;1803(2):191–200. doi:10.1016/j.bbamcr.2008.12.018 PubMed PMID: 19171166.
30. Fricke R, Gohl C, Bogdan S. The F-BAR protein family Actin' on the membrane. Commun Integr Biol. 2010 Mar;3(2):89–94. doi:10.4161/cib.3.2.10521 PubMed PMID: 20585497; PubMed Central PMCID: PMC2889961.
31. Hales KG, Korey CA, Larracuente AM, Roberts DM. Genetics on the Fly: A Primer on the Drosophila Model System. Genetics. 2015 Nov;201(3):815–42. doi:10.1534/genetics.115.183392 PubMed PMID: 26564900; PubMed Central PMCID: PMC4649653.
32. Gold KS, Brückner K. Macrophages and cellular immunity in Drosophila melanogaster. Semin Immunol. 2015 Dec;27(6):357–68. doi:10.1016/j.smim.2016.03.010 PubMed PMID: 27117654; PubMed Central PMCID: PMC5012540.
33. Afshar K, Stuart B, Wasserman SA. Functional analysis of the Drosophila diaphanous FH protein in early embryonic development. Development. 2000 May;127(9):1887–97. doi:10.1242/dev.127.9.1887 PubMed PMID: 10751177.
34. Coyle IP, Koh YH, Lee WCM, Slind J, Fergestad T, Littleton JT, et al. Nervous wreck, an SH3 adaptor protein that interacts with Wsp, regulates synaptic growth in Drosophila. Neuron. 2004 Feb 19;41(4):521–34. doi:10.1016/s0896-6273(04)00016-9 PubMed PMID: 14980202.
35. Tepass U, Fessler LI, Aziz A, Hartenstein V. Embryonic origin of hemocytes and their relationship to cell death in Drosophila. Development. 1994 Jul;120(7):1829–37. doi:10.1242/dev.120.7.1829 PubMed PMID: 7924990.
36. Bilancia CG, Winkelman JD, Tsygankov D, Nowotarski SH, Sees JA, Comber K, et al. Enabled negatively regulates diaphanous-driven actin dynamics in vitro and in vivo. Dev Cell. 2014 Feb 24;28(4):394–408. doi:10.1016/j.devcel.2014.01.015 PubMed PMID: 24576424; PubMed Central PMCID: PMC3992947.
37. Homem CCF, Peifer M. Exploring the roles of diaphanous and enabled activity in shaping the balance between filopodia and lamellipodia. Mol Biol Cell. 2009 Dec;20(24):5138–55. doi:10.1091/mbc.e09-02-0144 PubMed PMID: 19846663; PubMed Central PMCID: PMC2793291.
38. Schirenbeck A, Bretschneider T, Arasada R, Schleicher M, Faix J. The Diaphanous-related formin dDia2 is required for the formation and maintenance of filopodia. Nat Cell Biol. 2005 Jun;7(6):619–25. doi:10.1038/ncb1266 PubMed PMID: 15908944.
39. Suarez C, Kovar DR. Internetwork competition for monomers governs actin cytoskeleton organization. Nat Rev Mol Cell Biol. 2016 Dec;17(12):799–810. doi:10.1038/nrm.2016.106 PubMed PMID: 27625321; PubMed Central PMCID: PMC5125073.
40. Rotty JD, Wu C, Bear JE. New insights into the regulation and cellular functions of the ARP2/3 complex. Nat Rev Mol Cell Biol. 2013 Jan;14(1):7–12. doi:10.1038/nrm3492 PubMed PMID: 23212475.
41. Homem CCF, Peifer M. Diaphanous regulates myosin and adherens junctions to control cell contractility and protrusive behavior during morphogenesis. Development. 2008 Mar;135(6):1005–18. doi:10.1242/dev.016337 PubMed PMID: 18256194.
42. Kelley CF, Becalska AN, Berciu C, Nicastro D, Rodal AA. Assembly of actin filaments and microtubules in Nwk F-BAR-induced membrane deformations. Commun Integr Biol. 2015 Apr 29;8(2):e1000703. doi:10.1080/19420889.2014.1000703 PubMed PMID: 26478768; PubMed Central PMCID: PMC4594231.
43. O'Connor-Giles KM, Ho LL, Ganetzky B. Nervous wreck interacts with thickveins and the endocytic machinery to attenuate retrograde BMP signaling during synaptic growth. Neuron. 2008 May 22;58(4):507–18. doi:10.1016/j.neuron.2008.03.007

PubMed PMID: 18498733; PubMed Central PMCID: PMC2448395.
44. Zhai X, Shen Y, Zhang X, Li T, Lu Q, Xu Z. FCHSD2 cooperates with CDC42 and N-WASP to regulate cell protrusion formation. Biochim Biophys Acta Mol Cell Res. 2022 Jan;1869(1):119134. doi:10.1016/j.bbamcr.2021.119134 PubMed PMID: 34520816.
45. Rodal AA, Motola-Barnes RN, Littleton JT. Nervous wreck and Cdc42 cooperate to regulate endocytic actin assembly during synaptic growth. J Neurosci. 2008 Aug 13;28(33):8316–25. doi:10.1523/JNEUROSCI.2304-08.2008 PubMed PMID: 18701694; PubMed Central PMCID: PMC2546611.
46. Almeida-Souza L, Frank RAW, García-Nafría J, Colussi A, Gunawardana N, Johnson CM, et al. A Flat BAR Protein Promotes Actin Polymerization at the Base of Clathrin-Coated Pits. Cell. 2018 Jul 12;174(2):325-337.e14. doi:10.1016/j.cell.2018.05.020 PubMed PMID: 29887380; PubMed Central PMCID: PMC6057269.
47. Riedl J, Crevenna AH, Kessenbrock K, Yu JH, Neukirchen D, Bista M, et al. Lifeact: a versatile marker to visualize F-actin. Nat Methods. 2008 Jul;5(7):605–7. doi:10.1038/nmeth.1220 PubMed PMID: 18536722; PubMed Central PMCID: PMC2814344.
48. Wood W, Jacinto A. Drosophila melanogaster embryonic haemocytes: masters of multitasking. Nat Rev Mol Cell Biol. 2007 Jul;8(7):542–51. doi:10.1038/nrm2202 PubMed PMID: 17565363.
49. Théry M. Micropatterning as a tool to decipher cell morphogenesis and functions. J Cell Sci. 2010 Dec 15;123(Pt 24):4201–13. doi:10.1242/jcs.075150 PubMed PMID: 21123618.
50. Krause M, Gautreau A. Steering cell migration: lamellipodium dynamics and the regulation of directional persistence. Nat Rev Mol Cell Biol. 2014 Sep;15(9):577–90. doi:10.1038/nrm3861 PubMed PMID: 25145849.
51. Heckman CA, Plummer HK. Filopodia as sensors. Cell Signal. 2013 Nov;25(11):2298–311. doi:10.1016/j.cellsig.2013.07.006 PubMed PMID: 23876793.
52. Zhou C, Fan X, Zhang J. IRF3-mediated lncRNA FTX promotes cell proliferation, migration, invasion and suppresses cell apoptosis in oral squamous cell carcinoma by up-regulating FCHSD2 via miR-708-5p. Cell Mol Biol (Noisy-le-grand). 2023 Feb 28;69(2):31–6. doi:10.14715/cmb/2023.69.2.6 PubMed PMID: 37224049.
53. Stansley B, Post J, Hensley K. A comparative review of cell culture systems for the study of microglial biology in Alzheimer's disease. J Neuroinflammation. 2012 May 31;9:115. doi:10.1186/1742-2094-9-115 PubMed PMID: 22651808; PubMed Central PMCID: PMC3407712.
54. PrimerEfficiencyqPCR < Lab < TWiki [Internet]. [cited 2026 May 31]. Available from: https://barricklab.org/twiki/bin/view/Lab/PrimerEfficiencyqPCR
55. Bustin SA, Benes V, Garson JA, Hellemans J, Huggett J, Kubista M, et al. The MIQE guidelines: minimum information for publication of quantitative real-time PCR experiments. Clin Chem. 2009 Apr;55(4):611–22. doi:10.1373/clinchem.2008.112797 PubMed PMID: 19246619.
56. Jensen EC. Quantitative analysis of histological staining and fluorescence using ImageJ. Anat Rec (Hoboken). 2013 Mar;296(3):378–81. doi:10.1002/ar.22641 PubMed PMID: 23382140.

Some sections of this work were drafted with the help of the AI model Grammarly and Google Gemini. Any use of generative AI in this manuscript adheres to ethical guidelines for the use and acknowledgment of generative AI in academic research. The work has been thoroughly vetted for accuracy, and I assume responsibility for the integrity of this manuscript.

Acknowledgments – I would like to express my sincere gratitude to Prof. Dr. Bert Brône and Prof. Dr. Jean-Michel Rigo for welcoming me into the Brône-Rigo Neurophysiology lab at Biomed UHasselt and for their overall supervision throughout this project. A special word of thanks goes to Amber Delbroek, my daily supervisor, whose guidance, persistence, and enthusiasm for the research made this internship both scientifically rewarding and genuinely enjoyable. I am grateful for her continuous availability, thoughtful feedback, and for proofreading this thesis. I would also like to thank the other members of the research team for their support and assistance during the experiments. I am equally grateful to the BIOMED – Biomedical Research Institute at UHasselt for providing the facilities, resources, and technical support that enabled me to carry out this research. Finally, I acknowledge the Advanced Optical Microscopy Center at Hasselt University for their support with microscopy experiments, which was made possible by the Research Foundation Flanders (FWO).

Author contributions – AD and BB conceived and designed the research project. SVE and AD performed experiments, collected data, and analyzed it. SVE wrote the report, and AD revised it

Supplementary

Supplementary table 1: Oligonucleotide primer sequences used for qPCR. Forward and reverse primer sequences are provided in the 5' to 3' direction for the amplification of reference genes (*Rpl13a*, *Hprt1*) and target genes of interest (*Fchsd2*, *Diaph2*).

	Forward primer	Reverse primer
Rpl13a	5'-CACAAGACCAAGAGAGGCCA-3'	5'-CCACCATCCGCTTTTTCTTGT-3'
Hprt1	5'-ACAGGCCAGACTTTGTTGGA-3'	5'-ACTTGCGCTCATCTTAGGCT-3'
Fchsd2	5'-CTGTTCATCAGCAGCGGGTTC-3'	5'-CTGCTCGGCTCTGTTCTGATC-3'
Diaph2	5'-CTTCCTGACCAGAACGCACTC-3'	5'-CACCGTGCTCATCACAACAC-3'

Diaph2, diaphanous related-formin 2; *Fchsd2*, FCH and double SH3 domain 2; *Hprt1*, hypoxanthine phosphoribosyltransferase 1; *Rpl13a*, Ribosomal protein L13a.

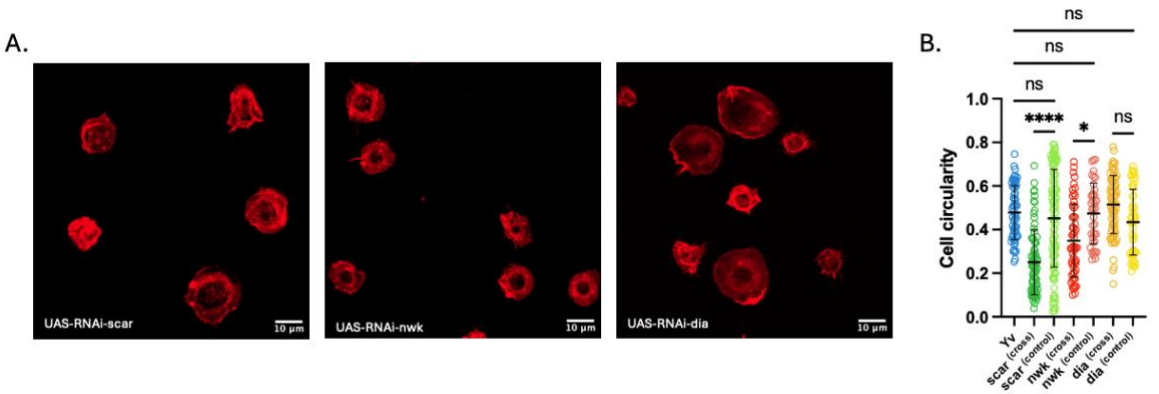

Supplementary figure 1: Aberrant cellular morphologies are induced by *dia* and *nwk* knockdown rather than UAS-constructs. Hemocytes containing the genotype Yv^1 (negative control), UAS-RNAi-*scar,* UAS-RNAi-*dia*, and UAS-RNAi-*nwk* were obtained from *Drosophila Melanogaster*. (**A**) Confocal microscopy images of primary hemocytes, isolated from *Drosophila melanogaster* third-instar larvae. Filamentous actin was visualized using phalloidin-647 iFluor staining (red). Imaging was performed using a Zeiss LSM 900 confocal microscope, and analysis was performed using Fiji. Scale bar represents 10 µm. (**B**) Quantification of cell circularity (0 = irregular, 1 = perfect circle). Data represent mean ± SD from six independent experiments. ****P < 0.0001, *P < 0.05, Kruskal-Wallis test followed by Dunn's multiple comparisons test. d*ia*, diaphanous; hemo, hemocyte; ns, not significant; *nwk*, nervous wreck; *scar*, suppressor of cAMP receptor; Yv^1, yellow vermillion.

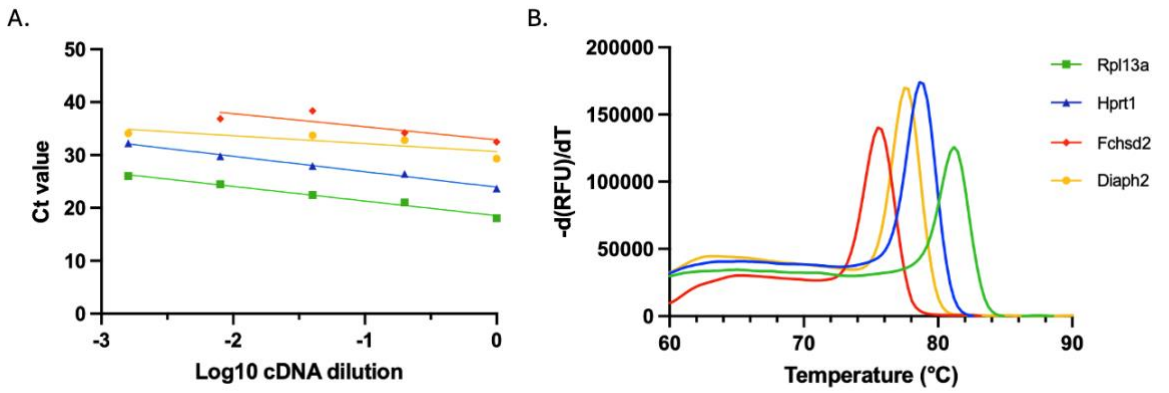

Supplementary figure 2: qPCR primers showed target-specific amplification in BV2 microglial cells. (**A**) Standard curve analysis for two reference genes (*Rpl13a*, *Hprt1*) and two target genes (*Fchsd2*, *Diaph2*). Cycle threshold values are plotted against log10-transformed relative cDNA dilution factors derived from a 5-fold serial dilution series of pooled BV2 cDNA (undiluted, 1/5, 1/25, 1/125, 1/625). Each data point (square, triangle, circle, diamond) represents a single reaction. Linear regression lines are colored according to the legend, each representing a single gene. (**B**) Melt curve analysis showing the negative derivative of fluorescence over temperature, plotted against the melting temperature (°C), for each primer set, with single measurements shown. cDNA, complementary DNA; ct, cycle treshold; *Diaph2*, diaphanous related-formin 2; *Fchsd2*, FCH and double SH3 domain 2; *Hprt1*, hypoxanthine phosphoribosyltransferase 1; RFU, relative fluorescent units; *Rpl13a*, Ribosomal protein L13a.

Supplementary table 2: Amplification efficiencies and standard curve metrics of qPCR primers in BV2 microglial cells. Parameters, including the slope, coefficient of determination (R^2), and calculated primer efficiency (%) derived from a 5-fold dilution standard curve, are represented for the reference genes (*Rpl13a*, *Hprt1*) and target genes (*Fchsd2*, *Diaph2*).

	Slope	R^2	Primer efficiency (%)
Rpl13a	-2.768	0.984	129.725
Hprt1	-2.921	0.992	119.953
Fchsd2	-2.480	0.722	153.071
Diaph2	-1.504	0.677	362.358

Diaph2, diaphanous related-formin 2; *Fchsd2*, FCH and double SH3 domain 2; *Hprt1*, hypoxanthine phosphoribosyltransferase 1; *Rpl13a*, Ribosomal protein L13a.

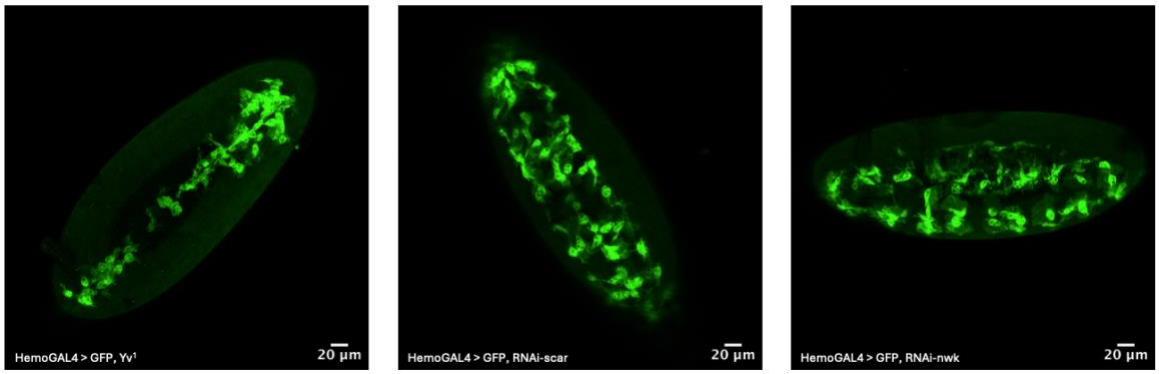

Supplementary figure 3: GFP does not clearly visualize hemocyte morphology *in vivo*. Confocal microscopy images showing the hemocytes in stage 15 *Drosophila melanogaster* embryos. The hemocytes are visualized using a HemoGAL4-driven GFP construct (green). *Drosophila melanogaster* strains were crossed to obtain embryos containing hemocytes with the genotype HemoGAL4 > GFP, Yv^1 (negative control), HemoGAL4 > GFP, RNAi-*scar* (positive control), HemoGAL4 > GFP, RNAi-*nwk* (target gene). Imaging was performed using a Zeiss LSM 880 confocal microscope, and analysis was performed using Fiji. Scale bar represents 20 µm. Hemo, hemocyte; *nwk*, nervous wreck; *scar*, suppressor of cAMP receptor; Yv^1, yellow vermillion.